

Research on the principle of space high-precision temperature control system of liquid crystals based Stokes polarimeter

Xin-Wei Zhang^{1,2}, Yang Zhang², Jia-Ben Lin², Jun-Feng Hou^{1,2} and Yuan-Yong Deng^{1,2}

¹ Key Laboratory of Solar Activity, National Astronomical Observatories, Chinese Academy of Sciences, Beijing 100101, China; jiabenlin@bao.ac.cn

² School of Astronomy and Space Science, University of Chinese Academy of Sciences, Beijing 101408, China

Received 2020 April 7; accepted 2020 July 14

Abstract The magnetic field is one of the most important parameters in solar physics, and a polarimeter is the key device to measure the solar magnetic field. Liquid crystals based Stokes polarimeter is a novel technology, and will be applied for magnetic field measurement in the first space-based solar observatory satellite developed by China, Advanced Space-based Solar Observatory. However, the liquid crystals based Stokes polarimeter in space is not a mature technology. Therefore, it is of great scientific significance to study the control method and characteristics of the device. The retardation produced by a liquid crystal variable retarder is sensitive to the temperature, and the retardation changes 0.09° per 0.1°C . The error in polarization measurement caused by this change is 0.016, which affects the accuracy of magnetic field measurement. In order to ensure the stability of its performance, this paper proposes a high-precision temperature control system for liquid crystals based Stokes polarimeter in space. In order to optimize the structure design and temperature control system, the temperature field of liquid crystals based Stokes polarimeter is analyzed by the finite element method, and the influence of light on the temperature field of the liquid crystal variable retarder is analyzed theoretically. By analyzing the principle of high-precision temperature measurement in space, a high-precision temperature measurement circuit based on integrated operational amplifier, programmable amplifier and 12 bit A/D is designed, and a high-precision space temperature control system is developed by applying the integral separation PI temperature control algorithm and PWM driving heating films. The experimental results show that the effect of temperature control is accurate and stable, whenever the liquid crystals based Stokes polarimeter is either in the air or vacuum. The temperature stability is within $\pm 0.015^\circ\text{C}$, which demonstrates greatly improved stability for the liquid crystals based Stokes polarimeter.

Key words: liquid crystals based Stokes polarimeter — high-precision temperature measurement — space high-precision temperature control — temperature field analysis — PID control

1 INTRODUCTION

The evolution of the solar magnetic field is the main reason for solar flares and coronal mass ejections (CMEs), which are the two most violent eruptions on the Sun. In order to study the origin of and possible causal relations among solar flares, CMEs and solar magnetic field activities, Chinese scientists have proposed the Advanced Space-based Solar Observatory (ASO-S) satellite (Gan et al. 2019) expected to be launched in 2021. It is the second batch of scientific experimental satellites determined by the space strategic pilot science and technology program of the Chinese Academy of Sciences. The Full-disk MagnetoGraph (FMG), one of the three main payloads

of the ASO-S satellite, will measure the full disk vector magnetic field with high spatiotemporal resolution and high magnetic field sensitivity (Deng et al. 2019). Polarization modulation is the core technology to realize measurement of the solar magnetic field. At present, the measurement of solar magnetic field is mainly based on the changes of Stokes parameters of polarized light via the Zeeman effect (Lin 2001), and then information on the solar magnetic field is retrieved by radiative transfer models of the solar atmosphere.

Mechanical modulation and electro-optical modulation are two common polarization modulation methods. The modulation velocity of mechanical components is low and cannot meet the requirements of high-sensitivity

magnetic field measurement for the FMG. The electro-optical modulator crystal includes KD*P, ferroelectric liquid and a nematic liquid crystal. A KD*P crystal is difficult to be used in space because of the complex structure of AC high-voltage modulation and silicone oil seal. The production process of a ferroelectric liquid crystal is complicated, and there is no report about its application in space. A nematic liquid crystal is driven by low voltage with a relatively simple structure, and its polarization sensitivity and precision can meet the needs of measurement of solar magnetic field. It is the major direction for future development and is expected to be adopted in the Solar Orbiter (Alvarez-Herrero et al. 2011) in 2020 (launched on 2020 Feb 10). Therefore, liquid crystals based Stokes polarimeter is the best choice for FMG to achieve high sensitivity polarization measurement. Thus, it is important to study its application, control and characteristics to realize the scientific target of FMG.

There are two liquid crystal variable retarders (LCVRs) that act as core optical elements in the liquid crystal based Stokes polarimeter. The retardation provided by LCVR is sensitive to the temperature, and the retardation changes 0.9 per 1°C . The error of polarization measurement caused by this change is 0.016, which affects the accuracy of magnetic field measurement. Therefore, the temperature stability of LCVR in a polarimeter is very important as it will directly affect the accuracy and validity of scientific data. FMG polarimeter will be operated in a vacuum under the condition of $22^\circ\text{C} \pm 2^\circ\text{C}$, the working temperature is 35°C and the temperature fluctuation is no more than 0.1°C (Deng et al. 2019). To achieve these targets, it is necessary to study the space high-precision temperature control system.

A lot of research has been done on high-precision temperature control systems. The temperature control system designed in the hydrogen atomic clock of the United States (Peng 2005) adopted the complex structure of three-stage temperature control, which can gradually improve the accuracy from the outside to the inside, and the temperature accuracy of the inner layer reached 10^{-4}°C . The temperature control system of a high-precision gravimeter designed by the Wuhan Seismological Bureau (Wu et al. 2008) has a stable accuracy of 0.0001°C , yet the system should be placed in a room with an accuracy of 0.1°C . The fuzzy PID control method adopted by Song & Fan (2001) made the accuracy of thermostatic bath with water or oil as the medium reach 0.01°C . Zhu et al. (2018) designed a high-precision temperature control system for optical crystals, whose accuracy was better than $\pm 0.002^\circ\text{C}$. The problem is the semiconductor cooler cannot be applied to an object with a complex structure. The chip, structure and thermal insulation material of the temperature control system in space are limited due

to the spatial environment. Yang et al. (2014) designed a space temperature control system with an accuracy of $\pm 0.03^\circ\text{C}$ based on the DSP PID algorithm for the space liquid bridge. However, the 24 bit analog-to-digital (A/D), utilized in this study to achieve high-resolution temperature measurement, is difficult to implement in space applications. The ASO-S satellite has an orbit of 720 km and its expected service life is no less than 4 years. It is necessary to use aerospace devices for a polarimeter due to the severe space environment. In recent years, there has been a great improvement in the temperature control system in the control circuits and algorithms. The integration degree of the control circuit is higher and the power consumption is lower. Compound control algorithms and neural network algorithms are widely implemented to make the control scheme more intelligent to complete more complex control tasks. However, it is still a challenge for a space temperature control system to reach high-precision.

In this paper, a high-precision temperature measurement circuit is designed by using low resolution A/D, which can be widely applied in aerospace applications. The temperature field of LCVR, which is more clearly understood as the thermal effect of light on LCVR, is analyzed theoretically. The temperature control algorithm of integral separation PI is utilized in the system to meet high-precision control requirements, which can satisfy the needs of the FMG polarimeter. Such research results have been applied to the development of FMG.

This article is organized in the following four parts. The first part introduces the principle of space high-precision temperature control, including the principle of space high-precision temperature measurement and control algorithm; the second part describes the system composition from three aspects: mechanical structure design, temperature control system hardware and software; the third part is about design of the temperature control experiment, and recording and analyzing the experimental data; the last part summarizes the full text and proposes an improvement for the system.

2 PRINCIPLES OF HIGH-PRECISION TEMPERATURE CONTROL IN SPACE

The temperature control system of a polarimeter requires a temperature control accuracy of 0.1°C . The key technology of the high-precision temperature control system is high-precision temperature measurement and the control algorithm. High precision temperature measurement is the premise of high precision temperature control, and temperature control algorithm is the kernel of high precision temperature control.

2.1 The Principle of High-precision Temperature Measurement in Space

High-precision temperature measurement is the premise of high-precision temperature control. A thermistor, installed as a temperature sensor, is connected to a Wheatstone bridge in the system. For thermistor temperature sensor, high resolution temperature measurement is equivalent to high resolution resistance measurement. The MF61 sensor used in this paper is a negative temperature coefficient thermistor (NTCR). Its resistance temperature curve (T - r curve) is expressed in Equation (1), where a , b , c and d are constants.

$$T = \frac{2c}{-b + \sqrt{b^2 - 4c(a - \ln r)}} - d. \quad (1)$$

The sensor is connected to the Wheatstone bridge (Wu et al. 1990) circuit. If the bridge reference voltage is V_{ref} , the bridge arm resistance is r and the bridge output voltage U is

$$U = V_{\text{ref}} \left| 0.5 - \frac{r}{R+r} \right|. \quad (2)$$

When the resistance of the sensor changes by Δr due to a small amount of temperature change ΔT , the output voltage of the bridge changes as

$$\begin{aligned} \Delta u &= V_{\text{ref}} \frac{\Delta r R}{(R+r)(R+r+\Delta r)} \\ &\approx V_{\text{ref}} \frac{\Delta r R}{(R+r)^2}. \end{aligned} \quad (3)$$

After it is amplified A times by the amplifying circuit, the voltage variation at the A/D input is $A\Delta u$, and the A/D range is U_R . In order to meet the temperature measurement with sufficient accuracy, the inequality that A should obey is

$$AV_{\text{ref}} \frac{|\Delta r|R}{(R+r)^2} \geq \frac{U_R}{2^B}. \quad (4)$$

At the same time, in order to meet the temperature measurement in a certain range, the following inequality should be satisfied

$$Au \leq U_R. \quad (5)$$

According to Equations (4) and (5), A satisfies

$$\frac{U_R}{2^B} \frac{(R+r)^2}{V_{\text{ref}} |\Delta r|R} \leq A \leq \frac{U_R}{V_{\text{ref}} \left| 0.5 - \frac{r}{R+r} \right|}. \quad (6)$$

Therefore, when the magnification A is increased, the temperature measurement accuracy is improved and the temperature measurement range is narrowed. When the magnification A is decreased, the case is opposite. With the programmable gain amplifier (PGA) selected, A changes dynamically according to output voltage U . At the same time, the temperature measurement with high-precision and wide range is realized.

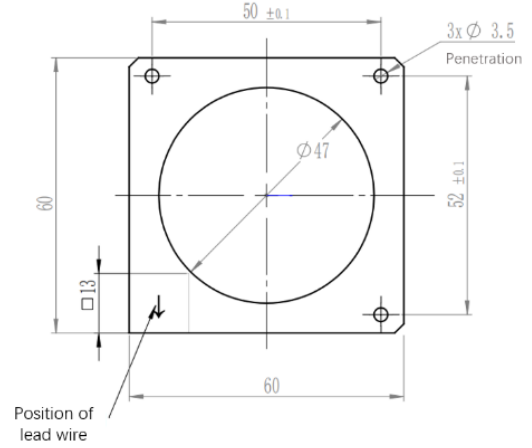


Fig. 1 A schematic drawing of heating film.

2.2 Temperature Control Algorithm and Control Mode

In view of the characteristics of polarimeter temperature control system, which requires high steady-state and low dynamic operation, the integral separation PI algorithm (Heredero et al. 2007) is selected as the main control mode. In this paper, as shown in Equation (7), when the set temperature is far higher than the actual temperature, that is, when the temperature difference δ is larger than a certain value c , the system relies on a certain constant maximum power P for heating; when the actual temperature exceeds a certain value b , the heating power is 0; when the temperature difference is small, PI control is used.

$$U(t) = \begin{cases} P & \delta > c > 0 \\ PI & c \geq \delta \geq -b \\ 0 & \delta < -b < 0 \end{cases}. \quad (7)$$

The temperature control algorithm outputs a floating-point number between 0 and 1, which is the PWM (Wu et al. 1990) duty cycle. PWM is widely implemented in temperature control systems to drive a heating wire or TEC. By increasing the minimum pulse frequency of PWM, the task of high-precision temperature control can be achieved. In this paper, polyimide heating films are used as the temperature control actuator. In order to achieve the best temperature control effect, the overall dimension of polyimide heating film, used as the temperature control actuator, is the largest area. The schematic drawing is displayed in Figure 1.

2.3 Thermal Analysis in Space

Ideally, when the polarimeter is at a constant temperature, the heat loss of the system is equal to the heat gain. In addition to the steady heat flow generated by the heating films, the heat gain also includes the heat effect generated by sunlight on the LCVR and radiated heat from the

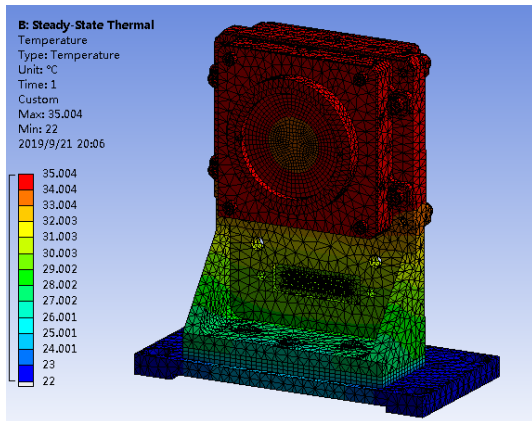


Fig. 2 Temperature distribution of liquid crystals.

environment. In a vacuum, heat loss occurs through heat conduction and radiation. Therefore, in order to satisfy the strength design of the space structure, reducing the contact surface between the structure and the box, and setting up heat insulation plate reduce the effect of heat conduction. At the same time, thermal radiation can be reduced by whitening the surface or applying anti-radiation materials. Thermal analysis of the polarimeter is done by ANSYS. Figure 2 features the temperature field distribution of the polarimeter in a 22° C vacuum. As illustrated in the figure, the temperature at the top of the polarimeter is higher and that at the bottom is lower; the temperature distribution range is 22.0 to 35.004° C.

As depicted in the right panel of Figure 3, it can be seen that the lowest temperature of LCVR appears at the bottom of the inner side (inward side) of the wave plate, where the heat dissipation is high due to the wire outlet. As shown in the figure, the white circle is the optical aperture of the LCVR. The temperature change of this part is the key point, which ranges from 34.206 to 34.817° C. According to the results of thermal analysis, there is a temperature gradient perpendicular to the bottom of LCVR, as pointed out by the arrow. The basic reason is that the upper and lower structures of the polarimeter are asymmetric, which results in different heat dissipation rates between the two surfaces. Therefore, in order to reduce the temperature gradient in this direction, the symmetrical polarimeter structure is redesigned or the heating film is added to the bottom of LCVR.

As shown in the Figure 4 below, the vertical temperature gradient decreases obviously, when 35° C heating films are added to the bottom of LCVR. The temperature range of LCVR aperture is 34.732 to 34.853° C, and the inhomogeneity is 0.121° C, far less than the previous 0.611° C.

For a further comparative study, the temperature fields of LCVR at 20° C and 24° C are analyzed, and the results are displayed in Table 1. It can be seen from the table that

with the change of vacuum temperature, the temperature field of LCVR also changes, and when the external temperature is lower, the temperature heterogeneity of LCVR is greater; when the heating film is added at the bottom of LCVR, the temperature field is more uniform. In addition, when there is no heating film on the bottom and the vacuum temperature changes from 20° C to 24° C, the lowest temperature of LCVR drift reaches $34.330-34.084 = 0.246^{\circ}\text{C}$, which exceeds the index of 0.1°C fluctuation of the project. When the heating film is added at the bottom, this parameter changes to $34.766-34.681 = 0.085^{\circ}\text{C}$, which meets the requirements. Therefore, through finite element analysis, we know that adding heating film at the bottom can not only make the LCVR temperature field more uniform, but also greatly reduces the LCVR temperature drift caused by the external temperature change. It can be predicted that when 35° C heating films are applied to the left and right sides of LCVR, the temperature field of LCVR will be more uniform and stable, but it also leads to more complex structures.

The meaning of the last column in Table 1 is the temperature of the position where the sensor is installed, which can represent the temperature of the sensor. Therefore, it can be seen that the temperature change of the sensor is weakly related to the installation position of the heating film and the vacuum temperature, and the maximum temperature change is less than 0.05°C . In other words, if we test the performance of the temperature control system, whether there is heating film on the bottom of LCVR or not, the experimental results have the same physical significance. Therefore, in the later temperature control system test experiment, heating film is not installed at the bottom of LCVR.

Because of the complex unsymmetrical structure design, finite element analysis is the main method that can analyze the effect of heat conduction and radiation. However, the approximate analytical solution of photothermal effect can be obtained under certain ideal assumption. When sunlight passes through LCVR, there will be a certain thermal effect inside, which will affect its temperature field. LCVR structure (Heredero et al. 2007) is shown in Figure 5. In the middle of the wave plate is liquid crystal materials. Polyimide layers, transparent indium tin oxide (IOT) electrodes, fused-silica substrates and the outermost anti-reflective (AR) coatings are symmetrically positioned from the innermost layer to both sides. Therefore, LCVR is a 9-layer composite structure consisting of five materials. To simplify the heat transfer model, the model of LCVR is transformed into a single-layer structure by neglecting the thin AR coatings, the IOT electrodes, liquid crystal material and the polyimide layers.

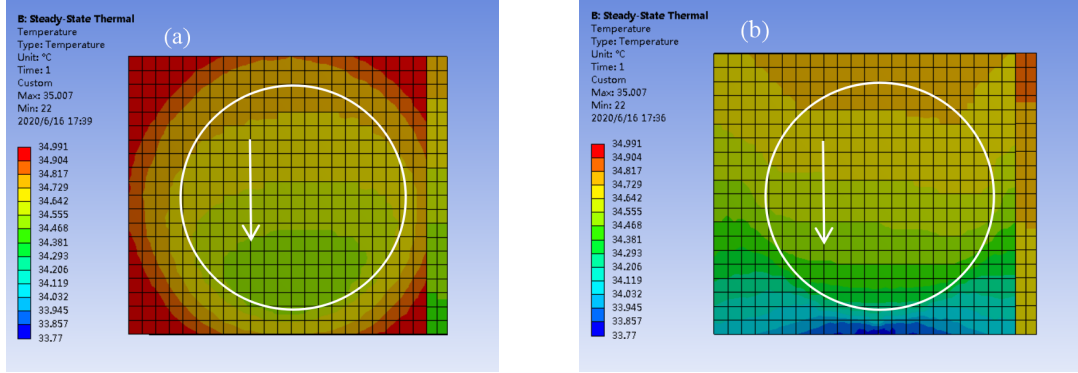


Fig. 3 Temperature distribution of outer side (a) and inner side (b) of LCVR.

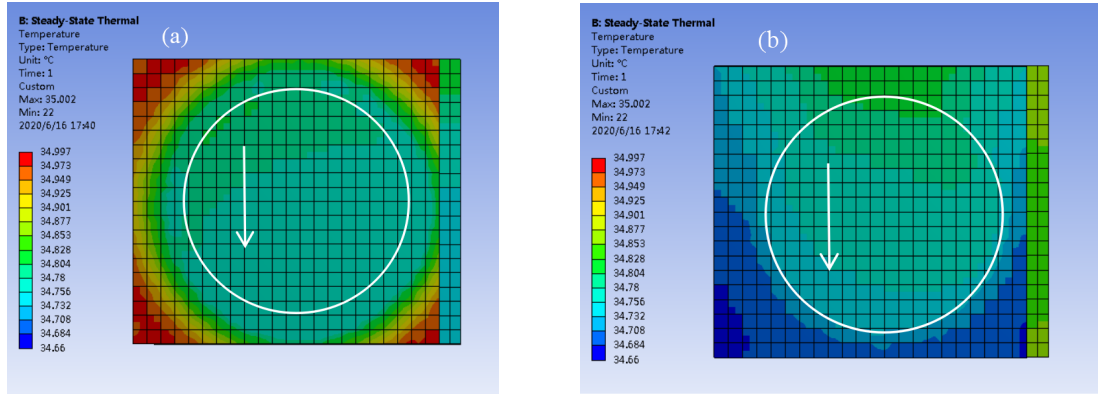


Fig. 4 Temperature distribution of outer side (a) and inner side (b) of LCVR with heating films on the bottom.

Table 1 LCVR Temperature Distribution under Different Simulation Settings

Simulation type	Vacuum temperature (° C)	Min temperature (° C)	Max temperature (° C)	Inhomogeneity (° C)	Sensor position temperature (° C)
No heating	20	34.084	34.788	0.704	34.919
film on	22	34.206	34.817	0.611	34.927
the bottom	24	34.330	34.844	0.514	34.936
With heating	20	34.681	34.824	0.143	34.941
films on	22	34.732	34.853	0.121	34.949
the bottom	24	34.766	34.871	0.105	34.958

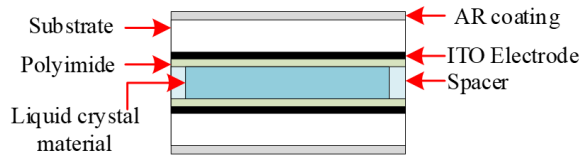


Fig. 5 Structure Diagram of LCVR.

The attenuation rate of light in a medium is directly proportional to the intensity of the light, when the light passes through a semitransparent homogeneous medium. α is the absorption coefficient of light; I_0 is the initial light intensity; I is the light intensity through the optical path x . If the light beam only transmits in the crystal, it can be

reflected as

$$\frac{dI}{dx} = -\alpha I. \tag{8}$$

On integration

$$I = I_0 e^{-\alpha x}. \tag{9}$$

Equation (10) expresses the light intensity at the x position in a translucent medium. Then, the intensity loss of the light at position x is

$$dI = -\alpha I_0 e^{-\alpha x} dx. \tag{10}$$

Assuming that the light loss intensity is dissipated in the form of heat, in the section with an area of S and at time t , the thermal energy Q generated by the light is

$$dQ = -dI * st = st\alpha I_0 e^{-\alpha x} dx. \tag{11}$$

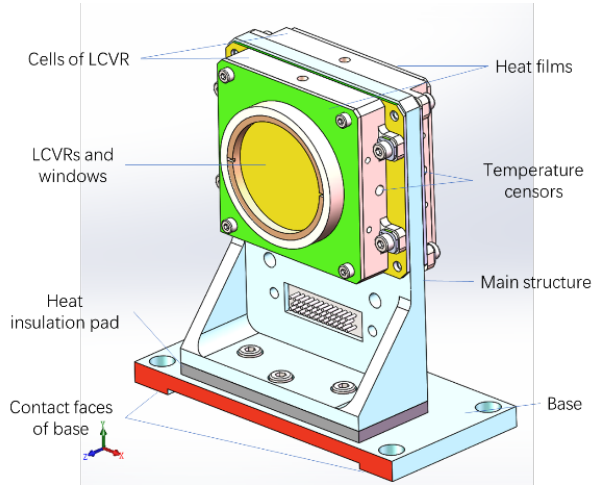


Fig. 6 Liquid crystals based Stokes polarimeter.

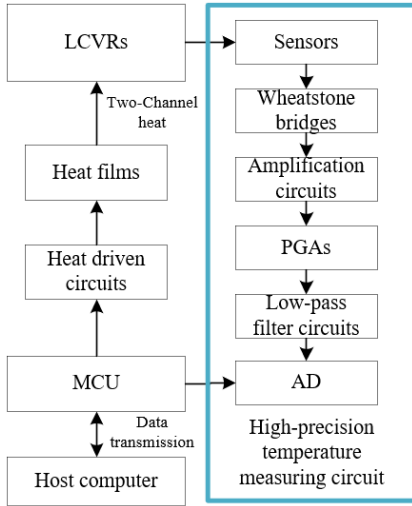


Fig. 7 Hardware block diagram of temperature control system.

That is to say, the intensity of the internal heat formed by the light is Φ_x

$$\Phi_x = \frac{dQ}{tdv} = \frac{dQ}{stdx} = \alpha I_0 e^{-\alpha x}. \quad (12)$$

In the steady-state condition, the differential equation of heat conduction of an infinite medium with a heat conduction coefficient λ satisfies the following requirement

$$\frac{d^2 t}{dx^2} + \frac{\Phi_x}{\lambda} = 0. \quad (13)$$

Then we get

$$t = \frac{I_0}{\alpha \lambda} e^{-\alpha x} + c_1 x + c_2. \quad (14)$$

Therefore, the influence of light on the temperature field of a homogeneous medium in a steady-state condition

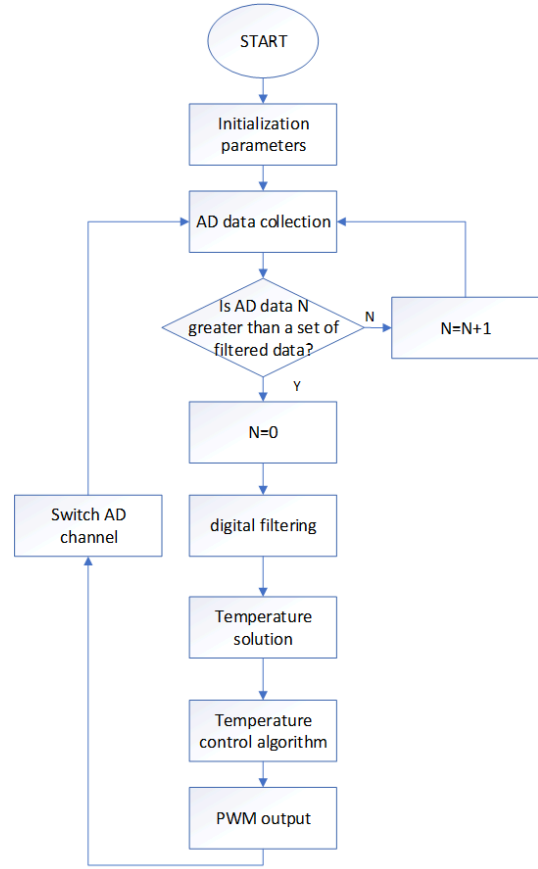


Fig. 8 Temperature control system flow chart.

is expressed in Equation (14). Ideally, the temperature distribution is only related to the thickness of LCVR. In this case, the temperature distribution in LCVR is from high to low from the incident surface to the exit surface, and the distribution of temperature field, ideally, ranges based on the negative exponential equation of natural constant. Based on the above inference, the temperature field of LCVR, with vertical light, can be described by Equation (14) under the condition that the light intensity, initial temperature and physical properties of each material in LCVR are known. It can also be seen from this formula that the main means to maintain the longitudinal uniformity of the temperature field of the LCVR and reduce the photothermal effect of LCVR are: adding insulating glass in front of the polarimeter and reducing the thickness of LCVR. The three different aspects above, high-precision temperature measurement, control algorithm and thermal analysis, are analyzed theoretically, then the hardware circuit, temperature control algorithm and heating scheme are determined. Thus, the key problem of high precision temperature control system is solved and the specific implementation will continue.

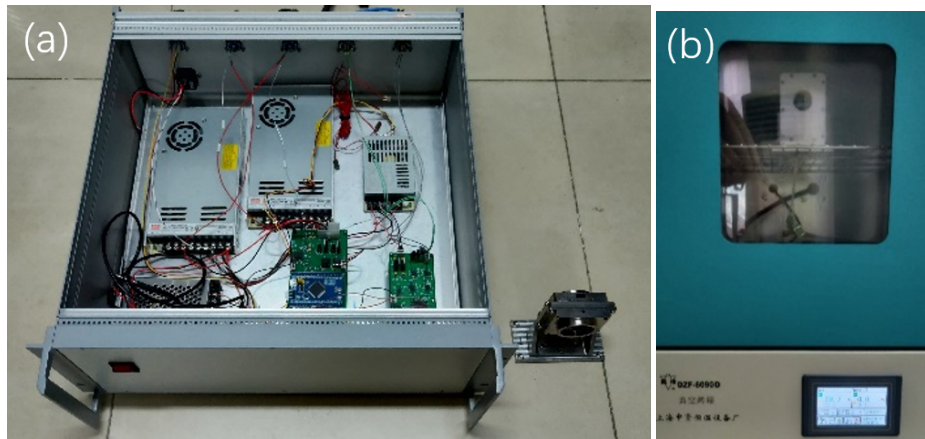


Fig. 9 Temperature experimental apparatus. (a) Control box and liquid crystals based Stokes polarimeter; (b) Vacuum chamber.

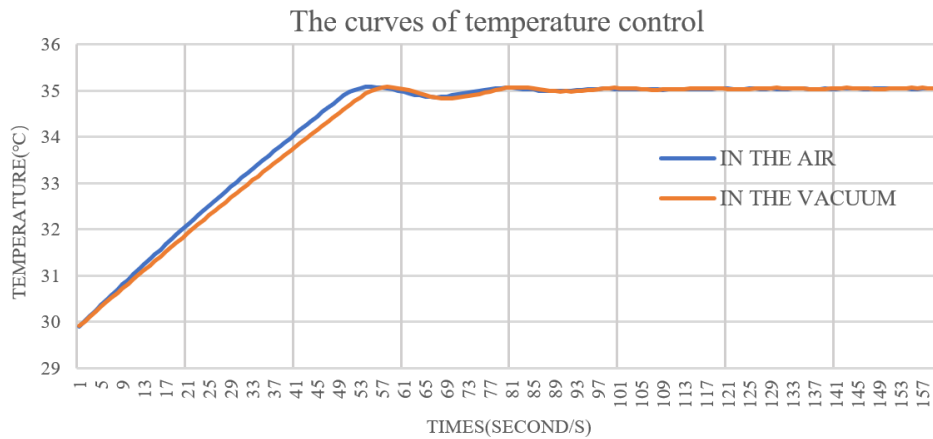


Fig. 10 Temperature control curves.

Table 2 Statistical Data on Temperature Control Experiment

Experimental type	No	Rise-time (s) (30~35°C)	Stationary time (s)	Average temperature °C	Max deviation °C
In air	1	51	51	35.0452	0.0141
	2	51	54	35.0345	0.0152
	3	51	52	35.0464	0.0152
In vacuum	1	54	65	35.0473	0.0236
	2	55	62	35.0482	0.0217
	3	54	63	35.0478	0.0250

3 DESIGN CONSIDERATIONS FOR THE SYSTEM

In space, weight and heat insulation are strictly limited, so the main frame of the polarimeter is designed with a titanium alloy single use technology. In order to reduce the heat conduction rate, a heat insulation pad is added between the main body and the base, and a convex structure is designed on the contact face of the base to reduce the contact area. To weaken the influence of thermal radiation, the outer surface of the structure is covered by

10 units of black carburized film. The structure of the polarimeter is illustrated in Figure 6.

The resolution of A/D commonly used in space projects is low because of the limitations imposed by electronic components on satellites, which cannot meet the design of a high-precision temperature measurement circuit. In order to obtain high-precision temperature (0.01° C resolution), the temperature acquisition circuit is mainly composed of sensors, Wheatstone bridges, amplification circuits, PGAs, low-pass filter circuits and 12-bit A/D. The control flow is realized by a microcontroller unit

(MCU), and MCU communicates with the host computer at the same time to transmit data and set parameters. PWMs are output and heating films are driven by heating circuits (maximum power 6 W) to realize high-precision temperature control. The system hardware block diagram is depicted in Figure 7.

The flow chart of the temperature control system is drawn in Figure 8. When the system starts to work, and the control parameters are initialized, the system firstly obtains the original data of channel 0 from AD, and carries out digital filtering after a group of filtered data is collected. The resistance and temperature of the thermistor are calculated by A/D data. Then the temperature control algorithm, using the temperature value, calculates the PWM duty cycle. Finally, the system outputs PWM and a control flow is completed. For the next cycle, it switches A/D channel, with temperature data acquired from the second channel, to start the other control flow.

4 TEMPERATURE CONTROL EXPERIMENT AND RESULTS

The circuit board was designed and debugged, and the experiment for temperature control system was done in air and vacuum. As featured in Figure 9, the control box and vacuum test box were operated in the experiment. In the room ($22^{\circ}\text{C}\pm 1^{\circ}\text{C}$) and in the vacuum ($22^{\circ}\text{C}\pm 1^{\circ}\text{C}$, 100 Pa), the temperature was set at 35°C , and the stability of the system was tested by three temperature control experiments. The curves of temperature control are plotted in Figure 10, and the statistical table of control characteristics is shown in Table 2. It can be seen from the table that the temperature control system operated stably and had high repeatability in the air. The first time to rise from 30°C to 35°C took about 51 s. After three fluctuations of 51~54 s, the maximum deviation is 0.0152°C . In vacuum, the three values are 50~52 s, 62~65 s and 0.0250°C . The results are much better than the project fluctuation index of 0.1°C . It can be inferred that when the ambient temperature becomes $20^{\circ}\text{C}\pm 2^{\circ}\text{C}$, even if the temperature fluctuation is estimated by a larger value, that is $2\times 0.0152 = 0.0304^{\circ}\text{C}$ and $2\times 0.0250 = 0.0500^{\circ}\text{C}$, these results meet the requirements for the project.

Therefore, either in the air or vacuum, the temperature control system has satisfied the requirements of high-precision. However, due to the change of environment, the rising time and the steady-state time of polarimeter temperature in vacuum are longer, and the temperature stability is slightly lower than that in the air.

5 CONCLUSIONS

In this paper, a high-precision temperature measurement circuit is formed by studying the principle of high-

precision temperature measurement; the temperature control algorithm of integral separation PI is determined by analyzing the heat transfer characteristics of polarimeter; and the optimal temperature heat scheme is proposed by finite element thermal analysis method. At last, a high-precision space temperature control system based on integral separation PI is designed. A comparative test in vacuum and air was carried out. The experimental results indicate that the system can achieve high-precision temperature control in both air and vacuum. In the air, the thermostatic stability of temperature control is better than $\pm 0.010^{\circ}\text{C}$, and in the vacuum, it is better than $\pm 0.015^{\circ}\text{C}$. The principle and scheme of high-precision and wide range temperature measurement circuit designed in this study can be widely applied in other space projects that necessitate high-precision temperature measurement.

Acknowledgements The authors would like to thank the support from these grants: the National Natural Science Foundation of China (Grant Nos. 11427803, 11427901 and 11773040), the Strategic Pioneer Program on Space Science, Chinese Academy of Sciences (CAS) (XDA04061002 and XDA15010800) and the Public Technology Service Center, National Astronomical Observatories of CAS (829011V01).

References

- Alvarez-Herrero, A., Uribe-Patarroyo, N., García Parejo, P., et al. 2011, Proceedings of SPIE - The International Society for Optical Engineering, 8160, 81600Y
- Deng, Y. Y., Zhang, H. Y., Yang, J. F., et al. 2019, RAA (Research in Astronomy and Astrophysics), 19, 157
- Gan, W. Q., Zhu, C., Deng, Y. Y., et al. 2019, RAA (Research in Astronomy and Astrophysics), 19, 156
- Herederer, R. L., Uribe-Patarroyo, N., Belenguer, T., et al. 2007, Applied Optics, 46, 689
- Lin, Y. Z. 2001, Introduction to Solar Physics (Beijing: Science press) (in Chinese)
- Peng, K. 2005, Graduate School of Chinese Academy of Sciences
- Song, M. G., & Fan, S. C. 2001, Journal of Beijing University of Aeronautics and Astronautics, 27, 560 (in Chinese)
- Wu, R., Dewan, S. B., Slemon, G., R. 1990, IEEE Transactions on Industry Applications, 26 880
- Wu, Y. X., Hu, G. Q., Jiang, Y. H., et al. 2008, Journal of Geodesy and Geodynamics, 28(5):133-135
- Yang, Z. Q., Li, X., & Xi, L. 2014, Computer Technology and Development, 24, 143 (in Chinese)
- Zhu, J. C., Dou, Z. W., Li, J. Q., et al. 2018, Optics and Precision Engineering, 26, 1604 (in Chinese)